



## Influence of support-layer deformation on the intrinsic resistance of thin film composite membranes



Masoud Aghajani<sup>a</sup>, Mengyuan Wang<sup>b</sup>, Lewis M. Cox<sup>c</sup>, Jason P. Killgore<sup>c</sup>, Alan R. Greenberg<sup>a</sup>, Yifu Ding<sup>a,b,\*</sup>

<sup>a</sup> Membrane Science, Engineering and Technology Center, Department of Mechanical Engineering, University of Colorado Boulder, Boulder, CO 80309-0427, USA

<sup>b</sup> Materials Science and Engineering Program, University of Colorado, Boulder, CO 80309-0596, USA

<sup>c</sup> Applied Chemicals and Materials Division, National Institute of Standards and Technology (NIST), Boulder, CO 80305, USA

### ABSTRACT

It is commonly believed that the overall permeation resistance of thin film composite (TFC) membranes is dictated by the crosslinked, ultrathin polyamide barrier layer, while the porous support merely serves as the mechanical support. Although this assumption might be the case under low transmembrane pressure, it becomes questionable under high transmembrane pressure. A highly porous support normally yields under a pressure of a few MPa, which can result in a significant level of compressive strain that may significantly increase the resistance to permeation. However, quantifying the influence of porous support deformation on the overall resistance of the TFC membrane is challenging. In particular, it is difficult to determine the deformation/strain of the membrane during active separation. In this study, we use nanoimprint lithography (NIL) to achieve precise compressive deformation in commercial TFC membranes. By adjusting the NIL conditions, membranes were compressed to strain levels up to 60%. SEM and AFM measurements showed that the compression had minimal impact on the barrier-layer surface morphology and total surface area with most of the deformation occurring in the support layer. DI water permeation measurements revealed that the water flux reduction decreases with an increase of strain level. Most significantly, the intrinsic membrane resistance showed negligible changes at strain levels lower than 30%–40%, but increased exponentially at higher strain levels, reaching 250%–500% of pristine (unstrained) membrane values. Using a resistance-in-series model, the strain dependency of the TFC membrane resistance can be described.

### 1. Introduction

TFC membranes are commonly used in reverse osmosis (RO) and nanofiltration (NF) processes for water desalination and reuse [1,2], as well as in emerging applications such as organic solvent nanofiltration (OSN). These membranes rely on an ultrathin, dense polyamide barrier layer atop a porous polymer support to allow for selective permeation. It was generally accepted that the porous support merely provided mechanical support for the barrier layer and contributed little or no resistance to permeate transport [3]. However, as the barrier layer thickness can now be as thin as 8 nm [4], the contribution of the porous support to the overall membrane resistance must be re-examined. Early work by Lonsdale et al. [5] showed that the influence of the porous support, particularly the surface porosity and pore size, on the diffusion length of the permeate through the barrier layer increases as the thickness of the barrier layer decreases. Recently, Ramon et al. [6] used 2D and 3D models to better understand the influence of the porous support. Their model showed that high permeability of the support material may significantly improve the overall permeability of the composite membrane. In addition, they showed that in current composite membranes, the location of the support pores creates a flux

distribution on the surface of the thin film.

The effects of the porous support can be amplified under the high hydraulic pressures (up to 7–8 MPa) used in RO to desalinate seawater, which can cause severe membrane deformation and correspondingly significant flux decline. The origin of this so-called compaction behavior remains unclear. Kurokawa et al. used a three-element model to describe the viscoelastic response of a cellulose acetate butylate RO membrane during compaction in an attempt to predict the corresponding flux decline [7]. Ohya developed a resistance-in-series model to describe the time-dependent flux of cellulose acetate membranes [8]. This model included both an exponential term for the porous support, which vanishes quickly after the start of the operation, and a linear term for the barrier layer, which governs long-term compaction. Peterson et al. [9] utilized ultrasonic time-domain reflectometry to simultaneously measure membrane displacement and flux decline during compaction. More recently, Hussain et al. [10] used a Voigt–Wiechert model to describe the deformation and permeation of TFC membranes with the assumption that the permeation rate is entirely controlled by the barrier layer. The same group compared the compaction behavior of a commercial NF membrane at low (< 2 MPa) and high (> 4 MPa) transmembrane pressures [11]. Within the low-pressure region, large

\* Correspondence to: Department of Mechanical Engineering, University of Colorado, 427 UCB, 1111 Eng. Drive, Boulder, CO 80309-0427, USA.

E-mail address: [Yifu.Ding@Colorado.Edu](mailto:Yifu.Ding@Colorado.Edu) (Y. Ding).

<https://doi.org/10.1016/j.memsci.2018.09.031>

Received 22 June 2018; Received in revised form 6 September 2018; Accepted 12 September 2018

Available online 13 September 2018

0376-7388/ © 2018 Elsevier B.V. All rights reserved.

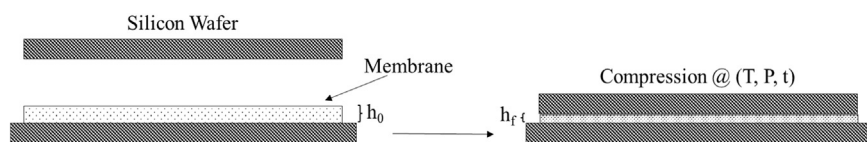
variation among the samples was observed, which was attributed to the heterogeneity of the barrier layer. When high transmembrane pressure was applied, the instantaneous compaction of the barrier layer reduced the heterogeneity and correspondingly the variability among samples. Porous membranes modified by incorporation of particles have been studied for different applications [12]. Pendergast et al. [13] showed that TFC membranes fabricated with a nanoparticle-reinforced polysulfone (PS<sub>f</sub>) support experienced less flux decline than membranes fabricated with an unmodified PS<sub>f</sub> support. This effect was attributed to better mechanical stability of the modified PS<sub>f</sub>, which results in less shrinkage of the surface pore opening and thus less increase in the permeate diffusion length through the barrier layer. However, under normal uniaxial compression, the surface pore size should show no change or slightly increase, as the Poisson's ratio of the porous support is typically in the range of 0–0.1 [14].

Beyond compaction, deformability of porous supports can be utilized to create well-defined surface patterns on a range of membranes [15–23]. The presence of such engineered roughness under fully wetted conditions can lead to enhanced surface shear during crossflow filtration and thus enhanced antifouling effects [18]. For TFC membranes, patterns can be either embossed on commercial membranes [19] or on the porous support followed by formation of the barrier layer [24]. In each approach, the porous support is significantly deformed, which likely affects the permselective performance of the TFC membrane.

Currently, the influence of TFC membrane deformation during high-pressure separation or surface patterning on the permeation resistance remains unclear. During compaction, the membrane continues to creep as the hydraulic pressure is applied, which makes it challenging to quantify the strain level. In contrast, NIL allows precise strains to be applied and measured. Herein, we applied NIL to initially compress TFC membranes to different strain levels, which allows quantification of the relationship between compressive strain and membrane resistance. For the three representative TFC membranes studied, we observed that the water flux reduction due to compaction monotonically decreases with the increase of initial strain level. The intrinsic membrane resistance against DI water permeation starts to increase substantially when the initial strain level is above ~ 40%. Based on our recent findings regarding a deformation-permeation relationship for porous membranes [25], the strain dependency of the permeation for TFC membranes can be described using a resistance-in-series model. The results presented here suggest that the resistance of the support can contribute substantially to the overall resistance of the TFC membranes at high strain levels.

## 2. Experimental

Four commercial membranes, three TFC and one ultrafiltration (UF), were used in this study: a NF membrane (NF-90, Dow FilmTec™), a brackish water RO membrane (TMGD, Toray Industries, Inc.), a seawater RO membrane (TMV, Toray Industries, Inc.), and a UF membrane (PW, GE Water). All the membranes were stored as received, and packages were resealed after each use. The polyester backing of the membranes was removed before further treatment and/or filtration. All characterization and DI water filtration experiments using the three TFC membranes were carried out with the barrier layer present atop the porous support. Both acetone and isopropanol were purchased from Fisher Scientific (Certified ACS grade with purity above 99.5%). Flux measurements were conducted using deionized (DI) ultrapure water (resistivity of 10 MΩ cm).



Dynamic mechanical analysis (DMA, TA Instruments Q800) was used to measure the glass transition temperature ( $T_g$ ) of the membranes. All tests were carried out over a temperature range of 30–250 °C at a rate of 5 °C/min with a strain amplitude of 0.1% and a dynamic load frequency of 10 Hz. For all of the membranes, rectangular samples with dimensions of 10 mm × 7 mm were used. The  $T_g$  of the samples was defined as the temperature at which the storage modulus was reduced by 50%.

The yield strength of the membranes was also determined by DMA using a uniaxial tensile test mode under isothermal conditions. For each membrane, measurements were carried out at both 40 °C and 150 °C under a constant strain rate of 0.01 min<sup>-1</sup>. Each sample was held at the designated temperature for 5 min before the measurement to ensure an isothermal condition throughout the sample was reached.

The barrier layer surface (top) and the cross section of the TFC membranes were imaged using field-emission scanning electron microscopy (FESEM, Supra 60, Zeiss). The cross-sections of the samples were prepared via fracture within a liquid nitrogen bath. To minimize charging effects, a 4–5 nm platinum layer was coated on all the samples prior to SEM imaging.

The surface topography of the TFC membranes was characterized with atomic force microscopy (AFM, Cypher, Asylum Research) from which the true surface area was calculated. All AFM measurements were performed in tapping mode under ambient conditions using a silicon cantilever with a backside Al reflex coating (Nanosensors, PointProbe® Plus). The scan size for all samples was 5 μm × 5 μm. The resolution (i.e. pixels and lines) of the scanned topographies was systematically increased until surface area measurements converged to a constant value for a given scan area which occurred at a pixel size of 10 nm × 10 nm.

Nanoimprint lithography equipment (NIL, Eitrie 3, Obducat, Sweden) was used for uniform initial uniaxial compression of the TFC membranes. As shown in Fig. 1, a membrane sample was placed between two identical silicon wafers (platens). The assembled fixture was compressed using an air-cushion technology to achieve highly uniform deformation across the membrane surface (1% variation over a 3-in. wafer diameter). By adjusting the pressure, temperature, and duration of the NIL process (summarized in Table S1), the membranes were compressed to different levels of strain. After the NIL compression, the samples were cooled to ambient temperature before the pressure was released.

Strain values ( $\epsilon$ ) for the compressed samples were determined by measuring the thickness of the samples before ( $h_0$ ) and after ( $h_f$ ) compression using an electronic micrometer (16426, HFS, resolution of 1 μm) and the following equation:

$$\epsilon = (h_f - h_0)/h_0 \quad (1)$$

For each sample, thicknesses at ten randomly selected locations were measured to obtain a mean value.

DI water permeation tests were carried out in a dead-end filtration cell (XX4504700, MilliporeSigma) with an active surface area of 9.6 cm<sup>2</sup> and pressurized with nitrogen. The permeate flow rate was measured with an automated electronic balance (TE2101, Sartorius) at 1-min intervals. For the NF-90, TMGD, and TMV membrane samples, DI water permeation was determined at 0.5 MPa, 0.97 MPa, and 1.45 MPa, respectively, unless otherwise specified; pressure values (all below the maximum operating pressure specified by the manufacturers) were chosen so that the initial permeate flow rate for each sample was similar and within the range of 1–1.5 ml/min. For each measurement, the

Fig. 1. Cross-sectional schematic of the initial membrane compression using NIL.

steady-state flux was defined as the flux with less than a 1% change over a 30-min interval. Time-dependent flux measurements to compare the compaction behavior of NF90 and PW membranes were carried out with DI water at 0.48 MPa. Before each permeation experiment, the membrane was soaked in an isopropanol/water solution (20:80 mixing ratio by volume) for 2 h to pre-wet the membrane; all experiments were conducted at room temperature.

For temperature sweep tests and tensile tests by DMA, data for one sample from each TFC membrane are reported. AFM scans were carried out on five randomly selected locations on the membrane surface with the mean and standard deviation reported. DI water filtration tests were carried out for at least three pristine samples of each TFC membrane; standard deviations for these measurements indicates the variability in the pristine samples. One DI water filtration measurement was carried out for each NIL-compressed sample. Time-dependent flux measurements for the NF90 and PW membranes were carried out for one sample from each membrane.

### 3. Results

#### 3.1. Mechanical properties of the commercial TFC membranes

Fig. 2a shows the storage modulus as a function of temperature from DMA measurements for the three TFC membranes. Note that the mechanical responses of the TFC membranes are dominated by the porous support (thickness 70  $\mu\text{m}$ –100  $\mu\text{m}$ ), and the contribution from the ultrathin barrier layer (thickness  $\sim$  150 nm–300 nm) [26] is negligible. For NF90, the behavior is similar to that of an amorphous polymer: as the temperature increases, the storage modulus remains approximately constant until it approaches the  $T_g$ , at which point the modulus starts to decrease significantly. For TMGD and TMV, similar glass transition behavior was observed. However, both membranes displayed a stiffening effect from 80  $^{\circ}\text{C}$  to 200  $^{\circ}\text{C}$ , which is most likely associated with the presence of proprietary additives within these commercial membranes (e.g. the pore-preserving agent; polymer additives used during the phase-inversion process). The  $T_g$  values for all membrane samples, are summarized in Table 1. All three membranes evidenced nearly identical  $T_g$ , suggesting that their porous supports are likely fabricated from a similar polymer. These  $T_g$  values are well within the range (190  $^{\circ}\text{C}$ –290  $^{\circ}\text{C}$ ) of PS<sub>f</sub> and polyethersulfone (PES), common support materials for TFC membranes [27]. It has been previously shown that compressing the porous supports at temperatures above the  $T_g$  of the polymer leads to detrimental pore-sealing [28] due to viscous flow of the polymer. Therefore, all NIL compression experiments were

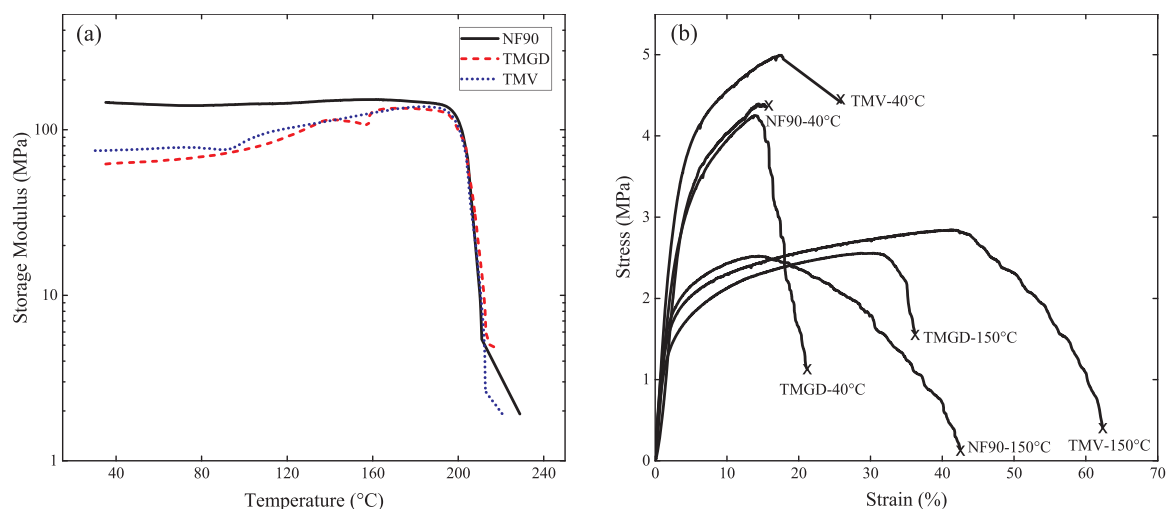
**Table 1**  
Thermo-mechanical properties of the TFC membranes obtained by DMA.

Membrane	$T_g$ ( $^{\circ}\text{C}$ )	Modulus (MPa) @ 40 $^{\circ}\text{C}$	Yield Strength (MPa) @ 40 $^{\circ}\text{C}$	Modulus (MPa) @ 150 $^{\circ}\text{C}$	Yield Strength (MPa) @ 150 $^{\circ}\text{C}$
NF90	203.6	100	3.4	110	2.1
TMGD	203.5	110	3.2	90	1.7
TMV	203.8	130	3.8	100	1.9

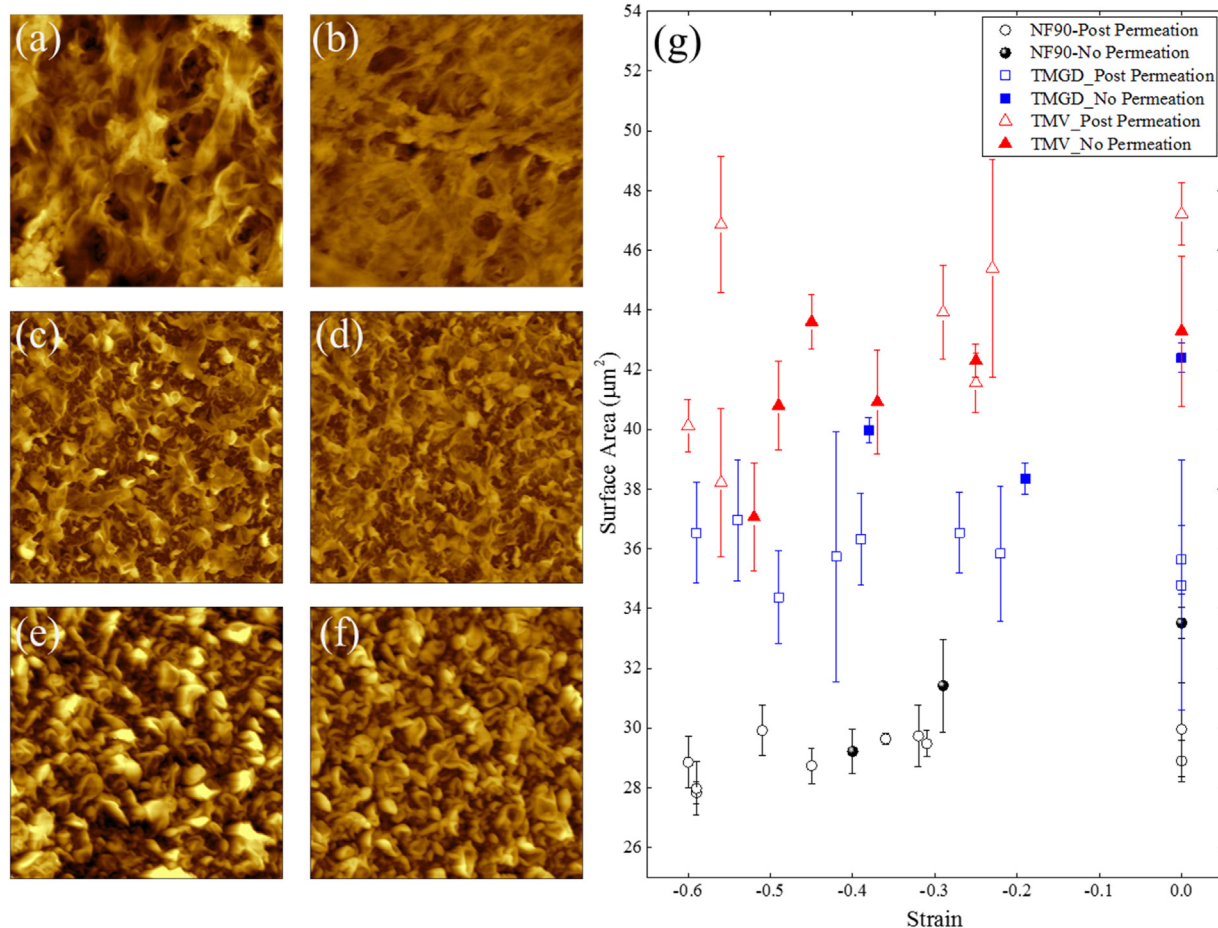
conducted within the range of 40  $^{\circ}\text{C}$ –150  $^{\circ}\text{C}$ , which is well below the  $T_g$  of the membranes.

Fig. 2b shows the stress-strain curves at a strain rate of 0.01  $\text{min}^{-1}$  for all three membranes at 40  $^{\circ}\text{C}$  and 150  $^{\circ}\text{C}$ , corresponding to the minimum and maximum of temperatures used for NIL compression. These curves evidence a viscoelastic behavior similar to that previously measured for PES UF membranes [29], confirming that the mechanical response of the TFC membranes are indeed dominated by their porous PES or PS<sub>f</sub> supports. From the initial elastic region (1%–2% strain), Young's modulus of the three membranes was estimated to be within the range of 90–130 MPa (Table 1), which is more than one order of magnitude lower than typical modulus values for glassy PS<sub>f</sub> or PES (around a few GPa). Interestingly, the stiffening effect observed for TMGD and TMV in the dynamic measurements (Fig. 2a) was not observed in the uniaxial tensile test. This suggests that additive(s) respond differently under low-amplitude dynamic loading (Fig. 2a) than uniaxial tension. The yield strength of each membrane,  $\sigma^*$ , can be estimated from these curves using a 2% off-set [30]. As summarized in Table 1,  $\sigma^*$  values at 150  $^{\circ}\text{C}$  were smaller than those at 40  $^{\circ}\text{C}$  for the same membrane, which is consistent with the response of a typical glassy polymer [31,32]. All three membranes displayed similar  $\sigma^*$  values at each temperature; these values are more than one order of magnitude lower than the bulk values for typical dense PS<sub>f</sub> or PES at the same temperatures [29]. The reductions in both Young's modulus and yield strength of the membranes from the corresponding bulk polymers are expected and caused by the porosity, which can be quantitatively described by an open-cell foam model [29].

Beyond yielding, further extension resulted in failure of the membranes at 40  $^{\circ}\text{C}$  (strain-at-failure  $\sim$ 15%–30%) and 150  $^{\circ}\text{C}$  (strain-at-failure  $\sim$ 35%–65%). For porous materials, the elastic deformation and stress plateau under uniaxial compression are comparable to those observed under uniaxial tension (Fig. 2b). More specifically, the yield strength under uniaxial compression is normally lower than that



**Fig. 2.** Thermomechanical properties of the three TFC membranes: (a) storage modulus as a function of temperature from DMA measurements; and (b) stress-strain curves at 40  $^{\circ}\text{C}$  and 150  $^{\circ}\text{C}$  measured under uniaxial tension at a rate of 0.01  $\text{min}^{-1}$ . The symbol “x” in (b) marks the failure point of the samples.



**Fig. 3.** (a), (c) and (e) are AFM topographic images of pristine NF90, TMGD, and TMV membranes; (b), (d) and (f) are AFM topographic images of compressed (60% strain) samples NF 90 (120 °C/40 bars), TMGD (150 °C/60 bars) and TMV (150 °C/60 bars). The color scale for all AFM images is  $-200$  nm to  $+200$  nm, darkest to brightest. (g) True surface area of the TFC membranes before and after NIL compression obtained from AFM measurements; the apparent surface area of all the membranes was  $25 \mu\text{m}^2$  (scan size:  $5 \mu\text{m} \times 5 \mu\text{m}$ ). Solid/open symbols correspond to AFM measurements on samples that have not/have been used in DI water permeation measurements, respectively. Standard deviation indicated by the error bars (For interpretation of the references to color in this figure legend, the reader is referred to the web version of this article.).

observed under tension [14]. This suggests that these TFC membranes will plastically deform under a pressure of a few MPa, which is well within the range of high-pressure RO. On the other hand, plastic deformation with varying strain levels in these membranes can be readily achieved by adjusting the compression conditions as used in this study (Table S1). Different from uniaxial tension, uniaxial compression will cause densification of the membranes instead of fracture [14].

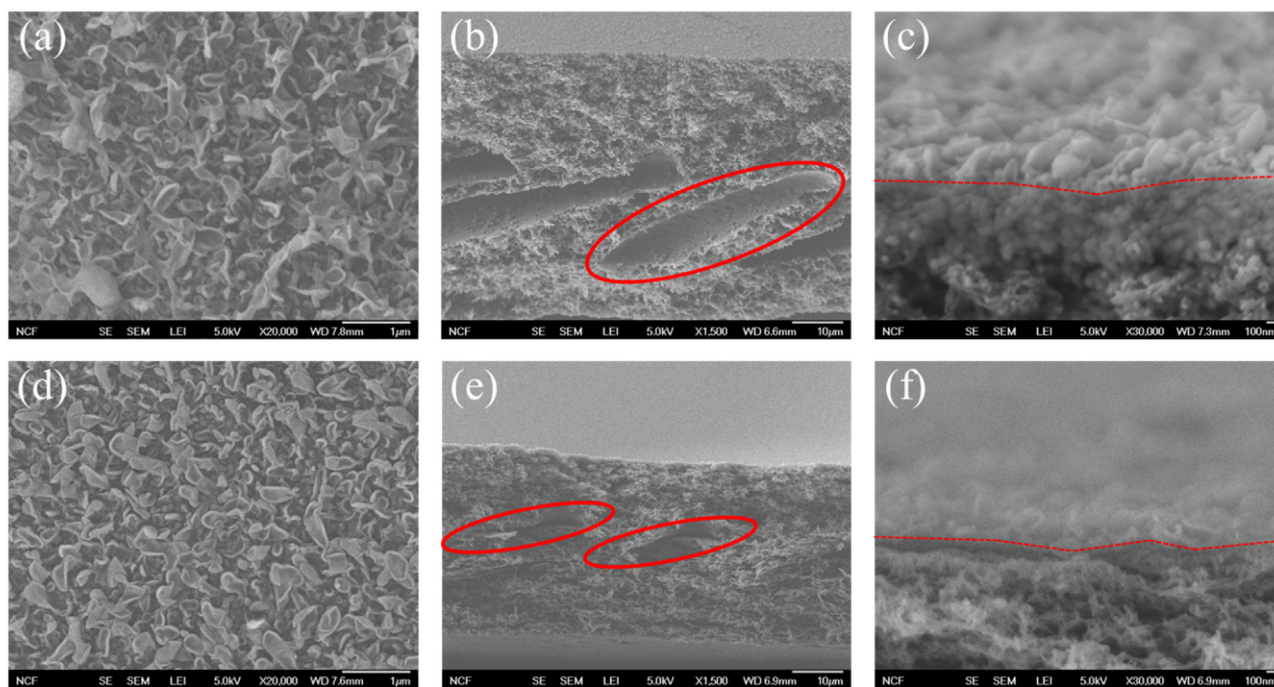
### 3.2. Surface and cross-sectional morphology

Fig. 3a–f show the representative topographic AFM images of pristine and highly compressed ( $\sim 60\%$  strain, the highest strain level used in this study) membranes. In contrast to the similarity in the thermo-mechanical responses (of the supports, Fig. 2), the three TFC membranes displayed characteristic barrier layer morphology. For pristine NF 90, the morphology of the barrier layer was predominantly collapsed structures (Fig. 3a). In contrast, pristine TMGD and TMV (Fig. 3c and e) membranes displayed more densely packed, deflated “balloon-like” protrusions with both lateral and vertical dimensions ranging from tens to hundreds of nanometers. Furthermore, these protrusions of the TMV barrier layer appear to be taller and thicker than those of the TMGD. All of these morphologies are commonly observed for TFC membranes and attributed to the interfacial polymerization process used to form the barrier layers [33,34].

Upon NIL compression with a Si wafer, despite deformation of some

of the taller features, no significant changes in the characteristic barrier layer morphologies were observed, as shown in representative AFM images (Fig. 3b, d, and f) for the three 60%-strained membranes. During NIL compression, the taller structures were the first ones in contact with the Si wafer and they tilted/bended under the pressure. In contrast, smaller features of the surface remained mostly unchanged due to better mechanical stability and/or protection by larger features leading to no or little contact with the Si wafer.

To quantify the compression effect, the “true” surface area, obtained from the topographic AFM measurements, was plotted as a function of the compressive strain for all of the TFC membranes (Fig. 3g). For pristine NF90, TMGD, and TMV samples, the true surface areas were  $34.6 \mu\text{m}^2$ ,  $42.5 \mu\text{m}^2$ , and  $43.5 \mu\text{m}^2$ , respectively, which correspond to 1.38, 1.7, and 1.74X that of the apparent surface area ( $25 \mu\text{m}^2$ ). These values were comparable to other reported AFM measurements on commercial membranes [35], but could be significantly lower than the actual total surface area of the barrier layer because of the inability of AFM to reach the embedded voids or undercut structures. Nevertheless, no significant changes in the true surface area were observed for the three membranes within the limitations of the AFM measurements. Specifically, the maximum reduction of the true surface area due to NIL compression was 13%, 9%, and 15% for NF90, TMGD, and TMV, respectively. No meaningful correlation between the strain level and the true surface area was detected. Furthermore, no significant differences in the AFM measurements were observed between samples used/not



**Fig. 4.** SEM images of TMV membranes before (a–c) and after (d–f) NIL compression at 120 °C and 4 MPa for 3 min (a) and (d) are the top-down view of the barrier layer. (b) and (e) are the cross-sectional view of the entire membrane in which the macrovoids are marked with a red oval. (c) and (f) are the cross-sectional view of the interfacial region between the barrier layer and the supports; the dotted line approximately shows the interface between the two layers (For interpretation of the references to color in this figure legend, the reader is referred to the web version of this article.).

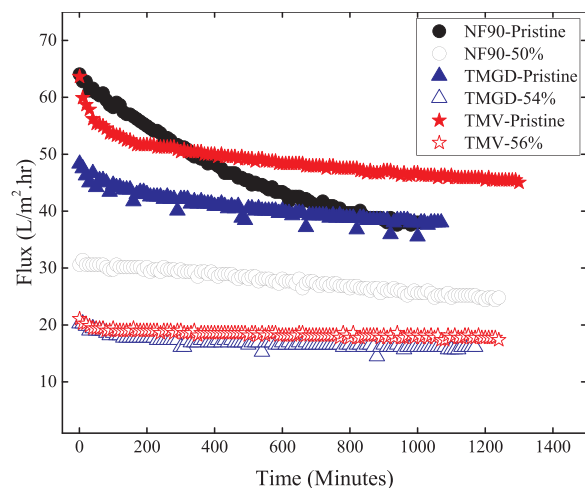
used for DI water permeation measurements.

Fig. 4a shows the top-down SEM image of the polyamide barrier layer on pristine TMV, confirming the typical RO membrane morphology as revealed by AFM (Fig. 3e). Similar to observations by AFM (Fig. 3f), the SEM images show that the larger protrusions were tilted during NIL compression while smaller nodules remain less affected (Fig. 4d). The porous support of the pristine membrane appeared to be asymmetric (Fig. 4b) with pore size gradually increasing with distance from the barrier layer side. Furthermore, finger-like macrovoids were present within the membranes. After NIL compression, severe densification of the porous support was observed (Fig. 4e), which reduced membrane thickness. Most significantly, the densification did not occur uniformly across the membrane thickness. Rather, the plastic deformation was more severe in regions with higher porosity and larger pores (near the bottom of the membrane) as evidenced by the complete crushing of the macrovoids that are circled in the cross-sectional views of the pristine and compressed samples (Fig. 4b and e). Within the limits of the SEM resolution, the regions near the barrier layer did not display significant plastic deformation (Fig. 4c to Fig. 4f).

Combining the AFM and SEM measurements, it is evident that most of the plastic deformation occurred in the porous support, specifically in regions with higher porosity and larger pore size. This type of non-uniform deformation is expected for asymmetric porous membranes under uniaxial compression [25]. Regions with higher porosity and larger pore size will have both lower elasticity and yield strength, and will experience more densification. In contrast, only modest changes in barrier layer morphology occurred as they are more mechanically robust.

### 3.3. Compaction behavior of compressed TFC membrane

DI water permeation experiments of all pristine and compressed membranes were carried out to quantify the influence of the membrane deformation on the permeation resistance. Fig. 5 shows the time-dependent DI water flux of both pristine and representative compressed samples for all three types of membranes. All pristine membranes



**Fig. 5.** Time-dependent DI water flux for the three TFC membranes: solid symbols represent pristine membranes, while empty symbols represent highly compressed membranes with strain level indicated in the inset. The permeation pressure was 0.5 MPa, 0.97 MPa and 1.45 MPa for NF90, TMGD and TMV membranes, respectively.

displayed compaction behavior, i.e. flux decline over time due to creep in the absence of fouling. Among them, NF 90 showed the largest water flux reduction due to compaction at the slowest rate, even though the lowest permeation pressure was used (0.5 MPa). For TMGD and TMV membranes, DI water flux showed a relatively rapid reduction followed by a slow decay. In contrast, all three compressed membranes evidenced a lower permeation flux, but also a much lower water flux reduction (Fig. 5). Clearly, deformation induced by NIL compression affects both the membrane structure and the permeation behavior.

Fig. 6a–c show the water flux reduction ( $\Delta J$ ), defined as the reduction in flux after 800 min of DI water permeation, as a function of strain for all three TFC membranes. For all three membrane types the

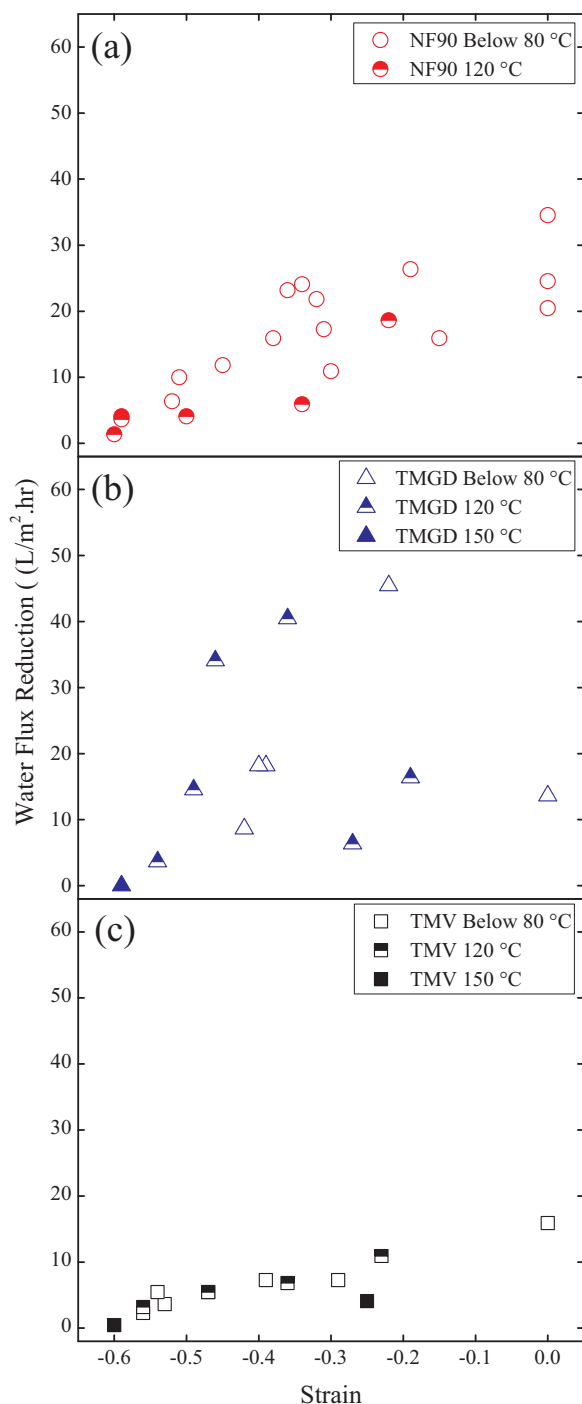


**Fig. 6.** Water flux reduction due to compaction, defined as initial flux minus the flux after 800 min of operation, for pristine and compressed samples of (a) NF90, (b) TMGD, and (c) TMV samples. For each membrane, different symbols represent the different temperature used in the NIL process.

experiments were carried out with the barrier layer present on top of the porous support. The  $\Delta J$  for TMV samples at all strain levels was considerably smaller than for NF90 and TMGD samples. Considering that the permeation pressure used for TMV (1.5 MPa) was greater than that for the other two membranes, the higher compaction resistance of TMV would likely be more evident if an identical permeation pressure were used. This is not surprising given that this membrane is designed to withstand high-pressure RO up to 8 MPa [1]. Overall, the response of all three membranes indicated that the  $\Delta J$  decreases with an increase of compressive strain. Specifically, highly compressed samples, e.g. strain

level between  $-0.5$  and  $-0.6$ , displayed very small  $\Delta J$  ( $0 \text{ L/m}^2 \text{ hr} - 4.5 \text{ L/m}^2 \text{ hr}$ ). Whereas the data for NF90 and TMV (Fig. 6a and c) tend to cluster suggesting a linear trend, the TMGD data are relatively scattered. Furthermore, there is no apparent influence of imprinting temperature on the  $\Delta J$  for membranes with similar compressive strain.

The porous supports of the TFC membranes, like the open-cell foams, can creep when subject to hydraulic pressure during separation. Normally, the presence of water within the membrane pores makes only a negligible contribution to the mechanical strength of the membrane in as much as the stress contribution from water is the multiplication of viscosity and strain rate, both of which are very low. For RO, the hydraulic pressure can reach a few MPa, which is comparable to the yield strength of the porous supports (Fig. 2b). Over an extended duration of high-pressure separation, the compressive deformation can be substantial. In situ measurements for the cellulose acetate (CA) membrane with a porosity as low as 36% under 4.1 MPa showed approximately 25% strain after 400 min [9]. Such compressive deformation is greatly accelerated during NIL processing where higher pressures and temperatures are used. Mechanically, membranes subjected to higher initial compressive strain will have higher mechanical strength due to reduced porosity of the porous support [25], and thus experience less deformation during DI water permeation. For example, it is a common practice in research studies to subject membranes to a pressure higher than the normal operating pressure for a specific duration in order to obtain a more stable flux for subsequent continuous operation [36]. Fig. 6 shows that TFC membrane strain, which occurred mostly within the support, is a good indicator for the water flux reduction during subsequent operation.

In addition to a lower  $\Delta J$ , compressed membranes showed lower permeation flux as compared with their pristine counterparts (Fig. 5). Intrinsic membrane resistance to DI water permeation ( $R$ ) was used to provide further quantitative insight via Eq. (2):

$$R = \left( \frac{Q_p}{A \cdot \Delta P} \right)^{-1} \quad (2)$$

where  $Q_p$  is the permeate flowrate at the steady state,  $A$  is the active surface area of the membrane, and  $\Delta P$  is the transmembrane pressure.  $R$  values of 0.12, 0.25, and 0.32 ( $\text{m}^2 \text{ hr bar/L}$ ) were calculated for pristine NF 90, TMGD, TMV membranes, respectively. Fig. 7 shows the normalized (by pristine membrane value) membrane resistance as a function of compressive strain. For all membrane samples the barrier layer was present on top of the porous support. There appears to be a NIL-temperature effect for all three membranes: at similar strain values, higher imprinting temperatures resulted in larger  $R$  values. This effect is more pronounced for TMGD and TMV membranes than for NF 90 membranes. For example, within the strain level of 20–40%, TMGD membranes compressed at 120 °C showed more than 75% higher resistance compared with those compressed below 80 °C. This behavior is likely related to the abnormal temperature dependency of the storage modulus for TMGD and TMV observed in DMA measurements (Fig. 2a). It is possible that these commercial membranes contain additives/modifiers in the porous support that segregate from the polymer cell wall, which cause membrane stiffening (Fig. 2a) and a certain degree of pore sealing. Regardless of the origin, this temperature behavior is undoubtedly caused by changes in the support rather than the thin barrier layer, as the mechanical measurements (Fig. 2a) are only sensitive to the supports. This observation also has direct implication for practical application of using NIL to pattern membranes: higher pressure is better than higher temperature to achieve membranes with similar strain (deformation) but lower resistance. Recently, Weinman et al. [19] have reported direct patterning of TFC membranes at 45 °C and 65 °C, which is well below the temperature ranges associated with a significant adverse effect. When compressed at temperatures below 80 °C (empty symbols in Fig. 7), all the three membranes displayed a similar trend: resistance of the membranes showed no meaningful

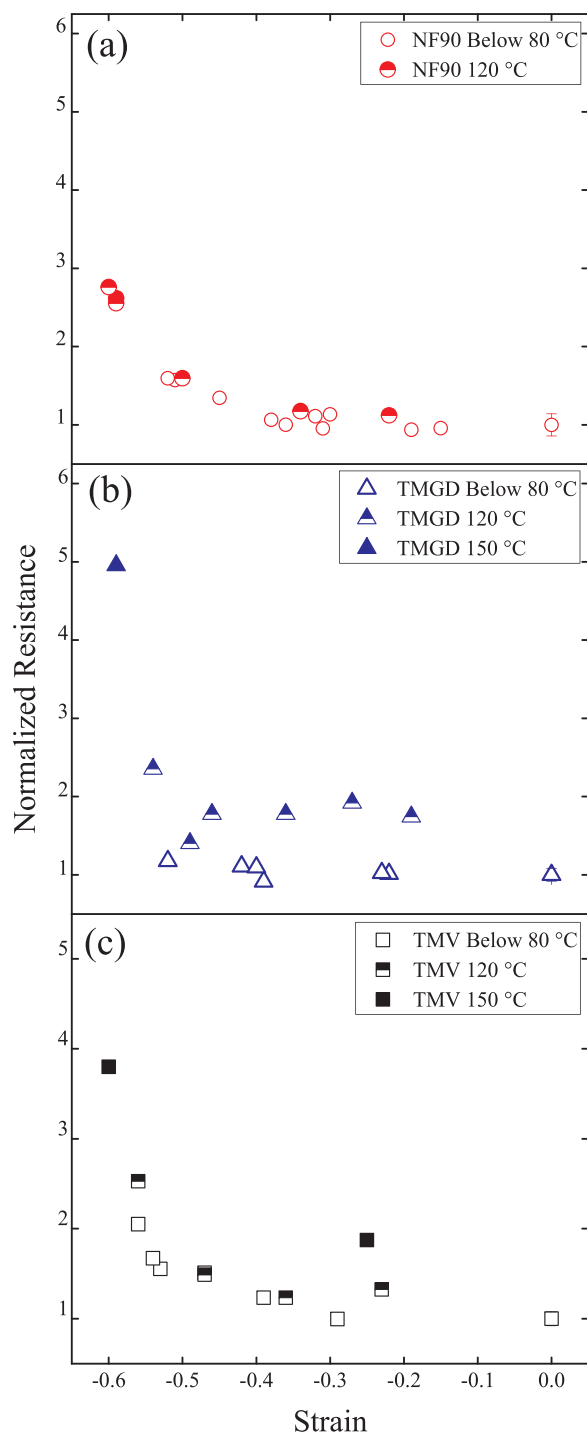


**Fig. 7.** Normalized resistance to DI water permeation as a function of compressive strain for pristine and compressed membranes: (a) NF90, (b) TMGD, and (c) TMV. Detailed NIL-compression conditions are provided in Table S1. Error bars for the pristine condition (initial strain = 0) represent the standard deviation ( $n \geq 3$ ), which is relatively small.

difference at strain levels lower than 40%, but clear differences were observed at higher strain levels. Interestingly, this strain level is comparable with the densification strain of the membrane ( $\varepsilon_D$ ) under compression, which marks the end of the stress plateau. For open-cell foams,  $\varepsilon_D = 1 - 1.4(\rho^*/\rho_0)$  [14], where  $\rho^*$  and  $\rho_0$  are the density of the porous structure and bulk polymer, respectively. According to this relationship, a porous support with an effective porosity of 60% has a  $\varepsilon_D$  of 44%.

#### 4. Discussion

A wide range of values for the permeability/permeance of TFC membranes including their corresponding porous supports have been reported [37–43]. Using a resistance-in-series model, the relative contribution of the porous support to the overall TFC membrane resistance in these studies ranges from 0.1% to 15%. Collectively, these studies indicate that the overall resistance of TFC membranes is dominated by the thin, dense barrier layer. However, the hydraulic pressures under which the TFC membranes and corresponding supports were tested typically differ by at least an order of magnitude and the conditioning times are often less than an hour [37,42,43]. Under high-pressure RO, substantial mechanical deformation is expected, which would lead to higher resistance than the value observed under lower pressure [44,45]. For example, Shi et al. [44] reported an 8% decrease in the DI water flux of a porous support as transmembrane pressure increases from 1.4 MPa to 1.6 MPa. Considering both the high pressure required for seawater desalination by an RO membrane (up to 8 MPa [1]) and the extended period of expected operation, the resistance of the porous support might be substantially higher than the value estimated using a typical UF operating pressure.

Fig. 8a compares the compaction behavior of NF 90 and PW, a typical UF membrane without a thin film barrier layer, both under a 0.5 MPa transmembrane pressure. The resistance of the PW membrane is less than 10% of that of the NF90 membrane prior to compaction. Over time, the resistance of both membranes increased monotonically, but the magnitude was much greater for PW. After about 8 h of operation, the resistance of the PW membrane increased to 27% of that of the NF 90 membrane. Undoubtedly, the water flux reduction for the PW membrane is expected to be even greater if higher transmembrane pressure is applied over a longer duration. Despite the difference in chemistry and pore structure between PW and the support of NF 90, the comparison in Fig. 8a suggests that the compaction and corresponding steady-state resistance of the supports could play a significant role during a high-pressure separation process.

The overall intrinsic resistance ( $R_T$ ) of TFC membranes can be modelled using a resistance-in-series model [8], as the sum of the resistance of the barrier layer ( $R_b$ ) and the porous support ( $R_s$ ). After NIL compression, most of the deformation is in the porous support. In our previous work [25], we showed that the influence of compressive strain on the permeability of porous polymeric membranes can be approximated by open-cell foam behavior, which is applicable to asymmetric UF membranes. Adopting this analysis for the porous supports and assuming no changes in  $R_b$  during the NIL compression, the intrinsic resistance of the compressed membrane as a function of strain ( $\varepsilon$ ) can be derived (detailed derivation is presented in the Supplementary material) as,

$$\hat{R}_T = \left[ x + (1-x) \left( \frac{1}{1+\varepsilon} \right)^{1.2} \right] \quad (3)$$

where  $\hat{R}_T$  is the overall resistance of the compressed TFC membrane normalized by that of the pristine membrane, and “ $x$ ” is the ratio  $R_b/R_T$  for the pristine membrane.

Fig. 8b plots the normalized resistance of the compressed TFC membranes as a function of compressive strain. Note that samples prepared with NIL temperatures above 80 °C were not included because of the additional temperature effects for the TMGD and TMV membranes. For comparison, two theoretical curves were also calculated using Eq. (3) and “ $x$ ” values of 0.9 and 0.7, i.e. assuming the barrier layer accounts for 90% and 70%, respectively, of the overall resistance of the pristine membrane. Qualitatively, each curve generally represents the trend of the experimental data, suggesting that the deformation of the porous support makes a substantial contribution to the overall resistance of the compressed TFC membranes, especially at higher strain levels.

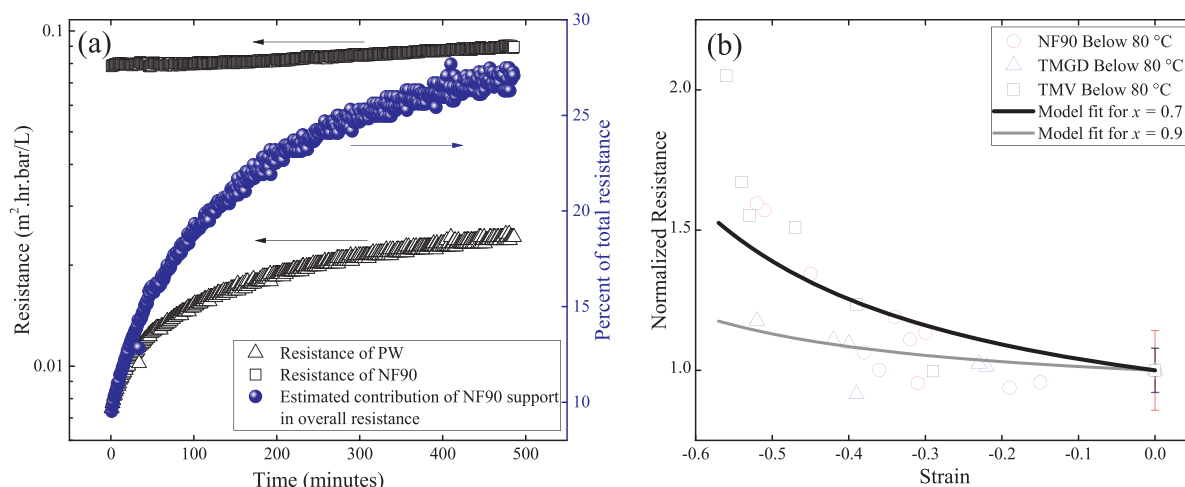


**Fig. 8.** (a) Resistance of NF90 and PW (an UF membrane) membranes during DI water permeation as a function of time (left axis) and estimated contribution of the porous support to the overall resistance of NF90 (right axis). The transmembrane pressure was 0.5 MPa for both membranes. (b) Normalized resistance of the three TFC samples along with predictions from Eq. (3) for two different values of  $x$ . Error bars indicate standard deviation for the unstrained condition.

In this study, the TFC membranes were compressed to different initial strain levels. In addition, the polymeric membranes undergo creep in response to the applied pressure driving permeation. In each case, the porous support deforms plastically due to the bending, twisting, and rotating of the polymer cell walls. However, during NIL compression at higher temperature and pressure, the polymer itself also plastically deforms, as the local stress is above the yield strength of the polymers. As a result, most of the plastic deformation that occurs during NIL compression is preserved after the load is released. In contrast, under high hydraulic pressure at room temperature, the local stress loading is below the yield strength of the polymer. Correspondingly, once the pressure is released, the deformed cell walls can spring back and no significant permanent deformation in the membranes is observed. In summary, the deformation of the porous support created by initial NIL compression is plastic (membrane)/plastic (polymer cell wall) whereas during high-pressure permeation the deformation is plastic (membrane)/elastic (polymer cell wall). It remains unclear whether membranes with an identical strain level, irrespective of whether achieved via NIL compression or hydraulic pressure, will have identical resistance.

Another important issue is whether the resistance of the barrier layer changes during NIL compression or hydraulic permeation. For a flat, dense polymer film, neither of the two mechanical loading scenarios should influence the transport resistance. However, the TFC membrane barrier layers display a series of extruded morphologies that could deform under mechanical loading (Fig. 3 and 4). In addition, recent studies revealed that the barrier layers could contain voids with varying size and shape [35,46–49]. Approximating this barrier layer as a porous material, similar plastic/plastic and plastic/elastic deformation is expected for both NIL compression and hydraulic permeation. From AFM and FE-SEM measurements (Fig. 3 and 4), no significant changes in the true surface area and morphology of the barrier layers were observed. Nevertheless, direct measurements of the barrier layer resistance will help confirm the validity of the resistance-in-series mechanism proposed here.

## 5. Conclusion

Porous supports are prone to mechanical deformation, which reduces porosity and increases permeation resistance. Such deformation-induced resistance changes in the support layer, which are normally negligible under low pressure, could affect the overall resistance of TFC membranes. In this study, we used NIL to deform TFC membranes to different controlled levels of initial strain, and quantified their intrinsic

membrane resistance and compaction behavior. Microscopic measurements by SEM and AFM showed no significant changes of the barrier-layer surface morphology and surface area while most of the strain was localized in the support layers. DI water permeation tests revealed that the water flux reduction due to compaction decreases with the increase of initial compressive strain. Most importantly, the intrinsic resistance of the membranes showed negligible changes at strain levels lower than 40%, but increased significantly at higher strain levels. The increased contribution of the support layer at high strain levels can be demonstrated by comparing the compaction behavior of a NF membrane with a UF membrane: the latter showed significant increases of membrane resistance under a relatively high operating pressure. Using a resistance-in-series model, the observed deformation-permeation relationship for the three commercial TFC membranes utilized in this study can be quantified. The results presented here suggest that the porous support can indeed contribute to the overall membrane resistance under high transmembrane pressures over long periods of operation. Therefore, the mechanical stability of the porous support is of critical importance, as it will define the maximum operating pressure of the membrane, which is often less discussed in the open literature. In addition, this insight also provides guidance for fabrication processes such as surface patterning that utilize mechanical deformation to create desired structures for improved performance.

## Acknowledgement

The authors gratefully acknowledge funding support from the National Science Foundation under Grant No. CBET-1264276, and IIP-1432952. The authors also gratefully acknowledge the National Science Foundation (NSF) Industry/University Cooperative Research Center for Membrane Science, Engineering and Technology (MAST) at the University of Colorado Boulder (CU-B) for support of this research via NSF Award IIP 1624602. The authors are also thankful for the partial support of Masoud Aghajani and Mengyuan Wang through the American Membrane Technology Association-United States Bureau of Reclamation (AMTA-USBR) fellowships.

Publications of NIST, an agency of the US government, are not subject to copyright. Certain commercial equipment, instruments, or materials are identified in this paper in order to specify the experimental procedure adequately. Such identification does not imply recommendation or endorsement by NIST, nor does it imply that the materials or equipment identified are necessarily the best available for the purpose.

## Appendix A. Supplementary material

Supplementary data associated with this article can be found in the online version at doi:10.1016/j.memsci.2018.09.031.

## References

- [1] L.F. Greenlee, D.F. Lawler, B.D. Freeman, B. Marrot, P. Moulin, Reverse osmosis desalination: water sources, technology, and today's challenges, *Water Res.* 43 (2009) 2317–2348.
- [2] G. Vaseghi, A. Ghassemi, J. Loya, Characterization of reverse osmosis and nano-filtration membranes: effects of operating conditions and specific ion rejection, *Desalin. Water Treat.* 57 (2016) 23461–23472.
- [3] J. Wang, D.S. Dlamini, A.K. Mishra, M.T.M. Pendergast, M.C. Wong, B.B. Mamba, V. Freger, A.R. Verliefe, E.M. Hoek, A critical review of transport through osmotic membranes, *J. Membr. Sci.* 454 (2014) 516–537.
- [4] S. Karan, Z.W. Jiang, A.G. Livingston, Sub-10 nm polyamide nanofilms with ultrafast solvent transport for molecular separation, *Science* 348 (2015) 1347–1351.
- [5] H. Lonsdale, R. Riley, C. Lyons, D. Carosella, Transport in composite reverse osmosis membranes, *Membrane Processes in Industry and Biomedicine*, 101 Plenum Press, New York, 1971.
- [6] G.Z. Ramon, M.C. Wong, E.M. Hoek, Transport through composite membrane, part I: is there an optimal support membrane? *J. Membr. Sci.* 415 (2012) 298–305.
- [7] Y. Kurokawa, M. Kurashige, N. Yui, A viscoelastic model for initial flux decline through reverse osmosis membrane, *Desalination* 52 (1984) 9–14.
- [8] H. Ohya, An expression method of compaction effects on reverse osmosis membranes at high pressure operation, *Desalination* 26 (1978) 163–174.
- [9] R. Peterson, A. Greenberg, L. Bond, W. Krantz, Use of ultrasonic TDR for real-time noninvasive measurement of compressive strain during membrane compaction, *Desalination* 116 (1998) 115–122.
- [10] Y.A. Hussain, M.H. Al-Saleh, A viscoelastic-based model for TFC membranes flux reduction during compaction, *Desalination* 344 (2014) 362–370.
- [11] Y.A. Hussain, M.H. Al-Saleh, S.S. Ar-Ratrou, The effect of active layer non-uniformity on the flux and compaction of TFC membranes, *Desalination* 328 (2013) 17–23.
- [12] M. Abolhassani, C.S. Griggs, L.A. Gurtowski, J.A. Mattei-Sosa, M. Nevins, V.F. Medina, T.A. Morgan, L.F. Greenlee, Scalable chitosan-graphene oxide membranes: the effect of GO size on properties and cross-flow filtration performance, *ACS Omega* 2 (2017) 8751–8759.
- [13] M.T.M. Pendergast, J.M. Nygaard, A.K. Ghosh, E.M. Hoek, Using nanocomposite materials technology to understand and control reverse osmosis membrane compaction, *Desalination* 261 (2010) 255–263.
- [14] L.J. Gibson, M.F. Ashby, *Cellular Solids: Structure and Properties*, Cambridge university press, 1999.
- [15] S.H. Maruf, A.R. Greenberg, J. Pellegrino, Y.F. Ding, Critical flux of surface-patterned ultrafiltration membranes during cross-flow filtration of colloidal particles, *J. Membr. Sci.* 471 (2014) 65–71.
- [16] S.H. Maruf, M. Rickman, L. Wang, J. Mersch, A.R. Greenberg, J. Pellegrino, Y.F. Ding, Influence of sub-micron surface patterns on the deposition of model proteins during active filtration, *J. Membr. Sci.* 444 (2013) 420–428.
- [17] S.H. Maruf, L. Wang, A.R. Greenberg, J. Pellegrino, Y.F. Ding, Use of nanoimprinted surface patterns to mitigate colloidal deposition on ultrafiltration membranes, *J. Membr. Sci.* 428 (2013) 598–607.
- [18] Y. Ding, S. Maruf, M. Aghajani, A.R. Greenberg, Surface patterning of polymeric membranes and its effect on antifouling characteristics, *Sep. Sci. Technol.* 52 (2017) 240–257.
- [19] S.T. Weinman, S.M. Husson, Influence of chemical coating combined with nano-patterning on alginate fouling during nanofiltration, *J. Membr. Sci.* 513 (2016) 146–154.
- [20] I.M.A. ElSherbiny, A.S.G. Khalil, M. Ulbricht, Surface micro-patterning as a promising platform towards novel polyamide thin-film composite membranes of superior performance, *J. Membr. Sci.* 529 (2017) 11–22.
- [21] J. Hutfles, W. Chapman, J. Pellegrino, Roll-to-roll nanoimprint lithography of ultrafiltration membrane, *J. Appl. Polym. Sci.* 135 (2018) 45993.
- [22] I.M. ElSherbiny, A.S. Khalil, M. Ulbricht, Surface micro-patterning as a promising platform towards novel polyamide thin-film composite membranes of superior performance, *J. Membr. Sci.* 529 (2017) 11–22.
- [23] S.H. Maruf, A.R. Greenberg, J. Pellegrino, Y. Ding, Fabrication and characterization of a surface-patterned thin film composite membrane, *J. Membr. Sci.* 452 (2014) 11–19.
- [24] S.H. Maruf, A.R. Greenberg, Y. Ding, Influence of substrate processing and interfacial polymerization conditions on the surface topography and permselective properties of surface-patterned thin-film composite membranes, *J. Membr. Sci.* 512 (2016) 50–60.
- [25] M. Aghajani, S.H. Maruf, M. Wang, J. Yoshimura, G. Pichorim, A. Greenberg, Y. Ding, Relationship between permeation and deformation for porous membranes, *J. Membr. Sci.* 526 (2017) 293–300.
- [26] V. Freger, Nanoscale heterogeneity of polyamide membranes formed by interfacial polymerization, *Langmuir* 19 (2003) 4791–4797.
- [27] S. Ida, PES (Poly (ether sulfone)), Polysulfone, *Encyclopedia of Polymeric Nanomaterials*, (2015), pp. 1528–1534.
- [28] O. Heinz, M. Aghajani, A.R. Greenberg, Y. Ding, Surface-patterning of polymeric membranes: fabrication and performance, *Curr. Opin. Chem. Eng.* 20 (2018) 1–12.
- [29] S.H. Maruf, Z. Li, J.A. Yoshimura, J. Xiao, A.R. Greenberg, Y. Ding, Influence of nanoimprint lithography on membrane structure and performance, *Polymer* 69 (2015) 129–137.
- [30] N.P. Cheremisinoff, *Handbook of Polymer Science and Technology*, CRC Press, 1989.
- [31] J. Richeton, S. Ahzi, K. Vecchio, F. Jiang, R. Adharapurapu, Influence of temperature and strain rate on the mechanical behavior of three amorphous polymers: characterization and modeling of the compressive yield stress, *Int. J. Solids Struct.* 43 (2006) 2318–2335.
- [32] C. Bauwens-Crowet, J. Bauwens, G. Homes, Tensile yield-stress behavior of glassy polymers, *J. Polym. Sci. Part B: Polym. Phys.* 7 (1969) 735–742.
- [33] S. Hermans, R. Bernstein, A. Volodin, I.F. Vankelecom, Study of synthesis parameters and active layer morphology of interfacially polymerized polyamide-polysulfone membranes, *React. Funct. Polym.* 86 (2015) 199–208.
- [34] F.A. Pacheco, I. Pinnau, M. Reinhard, J.O. Leckie, Characterization of isolated polyamide thin films of RO and NF membranes using novel TEM techniques, *J. Membr. Sci.* 358 (2010) 51–59.
- [35] M.M. Klosowski, C.M. McGilvery, Y. Li, P. Abellan, Q. Ramasse, J.T. Cabral, A.G. Livingston, A.E. Porter, Micro-to nano-scale characterisation of polyamide structures of the SW30HR RO membrane using advanced electron microscopy and stain tracers, *J. Membr. Sci.* 520 (2016) 465–476.
- [36] T.Z. Tong, S. Zhao, C. Boo, S.M. Hashmi, M. Elimelech, Relating silica scaling in reverse osmosis to membrane surface properties, *Environ. Sci. Technol.* 51 (2017) 4396–4406.
- [37] M. Son, H.-g. Choi, L. Liu, E. Celik, H. Park, H. Choi, Efficacy of carbon nanotube positioning in the polyethersulfone support layer on the performance of thin-film composite membrane for desalination, *Chem. Eng. J.* 266 (2015) 376–384.
- [38] N. Misdan, W. Lau, A. Ismail, T. Matsuura, Formation of thin film composite nanofiltration membrane: effect of polysulfone substrate characteristics, *Desalination* 329 (2013) 9–18.
- [39] S. Zhu, S. Zhao, Z. Wang, X. Tian, M. Shi, J. Wang, S. Wang, Improved performance of polyamide thin-film composite nanofiltration membrane by using polyethersulfone/polyaniline membrane as the substrate, *J. Membr. Sci.* 493 (2015) 263–274.
- [40] W. Yan, Z. Wang, J. Wu, S. Zhao, J. Wang, S. Wang, Enhancing the flux of brackish water TFC RO membrane by improving support surface porosity via a secondary pore-forming method, *J. Membr. Sci.* 498 (2016) 227–241.
- [41] M. Shi, Z. Wang, S. Zhao, J. Wang, S. Wang, A support surface pore structure reconstruction method to enhance the flux of TFC RO membrane, *J. Membr. Sci.* 541 (2017) 39–52.
- [42] A.K. Ghosh, E.M. Hoek, Impacts of support membrane structure and chemistry on polyamide-polysulfone interfacial composite membranes, *J. Membr. Sci.* 336 (2009) 140–148.
- [43] M.F. Jimenez-Solomon, P. Gorgojo, M. Munoz-Ibanez, A.G. Livingston, Beneath the surface: influence of supports on thin film composite membranes by interfacial polymerization for organic solvent nanofiltration, *J. Membr. Sci.* 448 (2013) 102–113.
- [44] Q. Shi, L. Ni, Y. Zhang, X. Feng, Q. Chang, J. Meng, Poly (p-phenylene terephthamide) embedded in polysulfone as substrate for improving compaction resistance and adhesion of thin film composite polyamide membrane, *J. Mater. Chem. A* 5 (2017) 13610–13624.
- [45] S. Stade, M. Kallioinen, A. Mikkola, T. Tuuva, M. Mänttäri, Reversible and irreversible compaction of ultrafiltration membranes, *Sep. Purif. Technol.* 118 (2013) 127–134.
- [46] F. Pacheco, R. Sougrat, M. Reinhard, J.O. Leckie, I. Pinnau, 3D visualization of the internal nanostructure of polyamide thin films in RO membranes, *J. Membr. Sci.* 501 (2016) 33–44.
- [47] H. Yan, X. Miao, J. Xu, G. Pan, Y. Zhang, Y. Shi, M. Guo, Y. Liu, The porous structure of the fully-aromatic polyamide film in reverse osmosis membranes, *J. Membr. Sci.* 475 (2015) 504–510.
- [48] M.C. Wong, L. Lin, O. Coronell, E.M. Hoek, G.Z. Ramon, Impact of liquid-filled voids within the active layer on transport through thin-film composite membranes, *J. Membr. Sci.* 500 (2016) 124–135.
- [49] L. Lin, R. Lopez, G.Z. Ramon, O. Coronell, Investigating the void structure of the polyamide active layers of thin-film composite membranes, *J. Membr. Sci.* 497 (2016) 365–376.